Bitlis Eren Üniversitesi Fen Bilimleri Dergisi
BİTLİS EREN UNIVERSITY JOURNAL OF SCIENCE
ISSN: 2147-3129/e-ISSN: 2147-3188
VOLUME: 12 NO: 2 PAGE: 307-319 YEAR: 2023
DOI:10.17798/bitlisfen.1181379

Co(II) Adsorption onto Ferrous Chloride and Thermally Modified Diatomite: Surface Properties and Adsorption Mechanism

Eda GÖKIRMAK SÖĞÜT[1*], Metin ÇELEBİ[1]

[1]*Van Güvenlik Meslek Yüksekokulu, Van Yüzüncü Yıl Üniversitesi, 65080 Van, Turkey*

(ORCID: 0000-0002-7707-3924) (ORCID: 0000-0003-1475-8878)

Keywords: Adsorption, Co (II), Ferrous chloride, Isotherms, Mechanism, Thermal treatment.

Abstract

As a potential alternative for heavy metal removal, adsorption using various low-cost materials is one of the most effective methods. This study presents the efficiency of local diatomite modified by ferrous chloride and heat treatment in removing Co(II) from an aqueous solution. The samples were characterized by ICP, XRD, TG-DTA, FTIR, SEM, and BET analyses and the adsorption efficiency of the samples for Co(II) ions was investigated under different factors such as contact time and pH. The adsorption equilibrium was well described by the Langmuir isotherm model, with the maximum adsorption capacities of D_A, D_M, $D_{M\text{-}550°C}$ and $D_{M\text{-}850°C}$ at about 18.18 mg L^{-1}, 28.65 mg L^{-1}, 48.30 mg L^{-1}, and 66.22 mg L^{-1}, respectively. The kinetic data were best fitted to the pseudo-second-order model. In addition, ion exchange and electrostatic surface complexation were predicted to play dominant roles in the adsorption mechanism. The results showed that the selected modification methods were effective in removing heavy metals from aqueous solutions, making the samples potentially cost-effective adsorbents to remove the water pollution problem.

1. Introduction

The advantages of developing technology to facilitate life lead to irreversible damage. Threats from numerous fields such as solid fuel consumption, exhaust emissions, domestic waste, mining and uncontrolled industrialization, rechargeable batteries, military, strategic, and critical industrial applications have started to provide negative notifications, especially for the natural environment [1], [2]. In particular, the pollution of water resources causes the waste to decompose during movement, causing irreversible damage to the environment and living beings [3]. It is a well-known fact that the concentration of heavy metals in wastewater, when the concentration significantly exceeds the limit of mg L^{-1}, has a toxic effect on all living things [1]. Among these heavy metals, the removal of cobalt (II) ions, which leads to the production of new-generation materials, is crucial for the future [2]. Cobalt and its salts are used in nuclear medicine, enamels, and semiconductors, in the coloring of glass and porcelain, in the hygrometer and electroplating, in the manufacture of vitamin B12, as a desiccant for lacquers, varnishes and dyes and as a catalyst for organic chemical reactions. Also, exposure to ionizing radiation is associated with an increased risk of developing cancer. The uncontrolled concentration of cobalt negatively affects all living species. It can cause paralysis, diarrhea, lung irritation, bone defects, and genetic changes in living cells [4]–[8]. Conventional methods such as membrane filtration [9], chemical precipitation [10], ion exchange [11], and adsorption [12] have been used to remove heavy metals from wastewater. Adsorption is the most widely used method with practical, economical, and recyclable properties. Industrial raw materials are widely used for adsorption applications [13], [14]. The main reason for this is the cheaper cost of industrial raw materials compared to production adsorbents and the financial contribution to the region [15], [16]. Among these industrial raw materials, fine-grained, physically and chemically inert diatomite, 80–90% of the pores consist mainly of amorphous

*Corresponding author: edagokirmak@yyu.edu.tr
Received: 08.09.2022, Accepted: 08.06.2023

silica (SiO_2. nH_2O), which consists of diatom shells. The diatomite surface has many active sites due to the silanol groups dispersed in the silica matrix [17]. These functional groups play a very active role in removing contaminants from the aqueous solution. Additionally, many modification processes are used to further functionalize the diatomite to increase its adsorption capacity. Modification methods are used, such as modification with transition metals, heat treatment, treatment with acids or bases, and organosilane. This leads to more attractive surfaces for adsorption [18], [19].

In this study, diatomite samples were first prepared by washing them with an acid solution for modification. In this study, environmentally harmless iron oxide was selected for surface modification of local diatomite. Iron oxide occurs naturally in several primary forms: ferrihydrite, hematite, goethite, lepidocrocite, and maghemite [20]. Ferrihydrite would be an optimal structure of iron oxide to modify diatomite due to its relatively high solubility in water for adsorption. In the ferrihydrite conversion process, a stable ferrihydrite should be preferred for the diatomite modification so that the adsorbed impurities are not released back into the solution over time. More Fe^{3+} vacancies caused by chemically absorbed Si^{4+} loosen the crystal lattice and inhibit the maturation and accumulation of Si^{4+} Fe-oxide particles. For this reason, stable ferrihydrite could be formed by Fe^{+2} oxidation in the presence of dissolved silica (Si). Dissolved silica could be prepared by treating crude diatomite with NaOH. Consequently, the dissolved Si provided by the diatomite contributes to the formation of stable ferrihydrite from the oxidation of Fe(II) [21], [22]. In the next step, ferrihydrite-modified diatomite samples were thermally treated at 550 ℃ and 850 ℃. The samples with enriched surface properties were characterized. Its effectiveness in the removal of heavy metals from aqueous solutions was investigated, and its possible mechanism was interpreted.

2. Materials and Method

2.1. Materials

Raw diatomite samples obtained from the Çaldıran-Van region were ground and sieved to 350 mesh particle size, washed with distilled water, and then dried at 100 °C. The chemical composition of diatomite is mainly SiO_2 (69.70%) [18]. All the chemicals (Ferrous chloride ($FeCl_2$) 98%, NaOH 98%, HCl %37, $AgNO_3$ 99%, KNO_3 99%, HNO_3 70%, and $Co(NO_3)_2.6H_2O$ were purchased from Sigma Aldrich, and no purification was performed.

2.2. Preparation of adsorbents

The diatomite sample was stirred with a 2 M HCl solution at 105° C for 4 hours. At the end of this process, it was washed several times to ensure Cl^- (tested by AgNO3) was removed and named as D_A. 90° C was dried in the oven and stored in a clear glass jar with a lid. Then, in step 15, g of D_A were mixed with 6 M NaOH at 80° C for 2 hours. The mixture was added to 1 M $FeCl_2$ by keeping the pH between 1 and 2 using HCl, and stirring was continued at room temperature for 10 hours. To increase the rate of formation of iron (II) hydroxide, the sample was treated again with 6 M NaOH at room temperature for 6 h, filtered, washed several times with distilled water, and dried in a drying oven at 105 °C. The resulting sample was named as D_M and stored in a clear glass jar with a lid. In the final step, the D_M sample was thermally treated at 550 °C and 850 °C for 3 hours. These samples were named as $D_{M\text{-}550°C}$ and $D_{M\text{-}850°C}$ and kept for later use in a clear glass jar (Scheme 1).

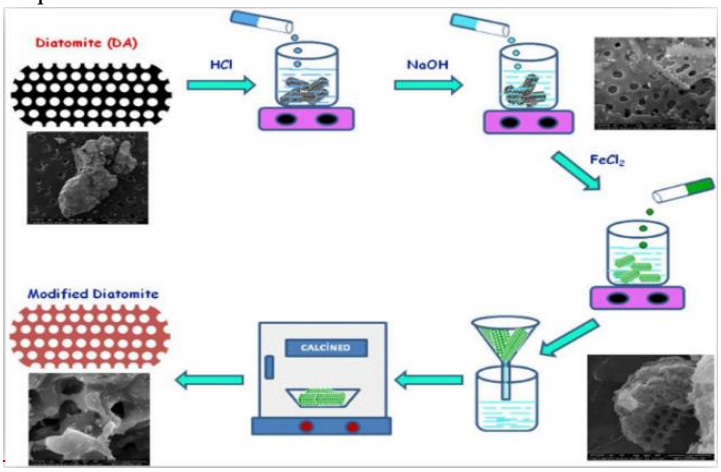

Scheme 1. Scheme of the process for the preparation of modified diatomite.

2.3. Preparation of Co (II) ion solutions

A $Co(NO_3)_2.6H_2O$ stock solution (1000 mg L^{-1}) was prepared with distilled water. It was diluted at different concentrations in the range of 10-50 mg L^{-1}.

2.4. Characterization of the adsorbents

D_A, D_M, $D_{M\text{-}550°C}$, and $D_{M\text{-}850°C}$ materials were characterized by Inductively Coupled Plasma Optical Emission Spectrometer (ICP-OES, Perkin Elmer Optima 4300DV), X-ray diffraction analysis (XRD, Philips PW 1830-40 with Cu-K radiation), Thermal analysis using a thermal analyzer (TG-DTA, Rigaku 2.22E1), Fourier transform infrared measurement (FT-IR, Bio-Rad Win-IR spectrometer at a resolution of 2 cm^{-1} in KBr pellet at room temperature), and Scanning Electron Microscopy (SEM), Multi-point BET Analysis (Quantachrome Nova 2200E Surface Area & Pore Size Analyzer), and Mastersizer analysis (Malvern) the zero point of charge (pH_{zpc}) of adsorbents were obtained by mass titration [18].

2.5. Batch Adsorption Experiments

The adsorption nature of the samples, the effects of changing contact times (1-120 min.), concentration, and pH (2-9) change were observed. The effect of pH was examined dropwise by adding 0.1 M NaOH or 0.1 M HCl solutions. Experiments were performed on a thermal shaker at a controlled temperature (298 K) using 20 ml glass vials containing 0.1 mg adsorbent and 10 mL of different concentrations (10-50 mg L^{-1}) of adsorbent (in Scheme 2).

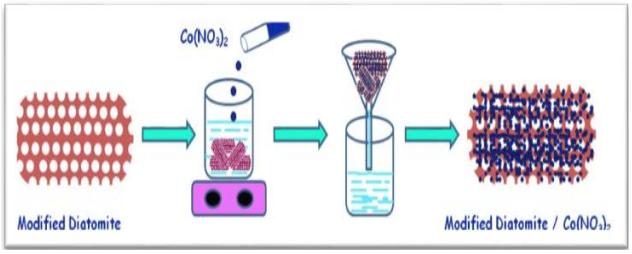

Scheme 2. Schematic illustration of Co (II) adsorption process.

In the last step, the adsorbents were removed by centrifugation. In the analysis of adsorption data, the percentage of removal (% Removal) was calculated according to Eq. 1;

$$\%R = \frac{C_0 - C_e}{C_0} \times 100\% \quad (1)$$

The adsorption capacity (q_e) (mg g^{-1}) was calculated using Eq. 2;

$$q_e = \frac{(C_0 - C_e)\,V}{m} \quad (2)$$

where q_e (mg L^{-1}) is the equilibrium adsorption capacity of the adsorbent, C_0 and C_e (mg L^{-1}) are the initial and final concentrations of the Co (II) ions quantity in solution, V (mL) is the volume of solution and m (mg) is the mass of D_A, D_M, $D_{M\text{-}550°C}$, and $D_{M\text{-}850°C}$ used.

Equilibrium data were applied to Langmuir, Freundlich, and Dubinin-Radushkevich isotherm models. Pseudo-first-order (PFO) and second-order (PSO) models, intraparticle diffusion models, and the Boyd model were applied to define adsorption behavior. The equations for all models are presented in Tables S1-2.

3. Results and Discussion

3.1. Characterizations of Adsorbents

The change in percentages of diatomite compounds in different regions depends on geological effects. The rates of diatomite obtained in the Van-Çaldıran region are presented in a previous study [18]. The compound percentages of the D_A, D_M, $D_{M\text{-}550°C}$, and $D_{M\text{-}850°C}$ samples obtained are presented in Table 1.

Table 1. Oxide Content (% weight) in D_A, D_M, $D_{M\text{-}550°C}$ and $D_{M\text{-}850°C}$

Chemical Composition	D_A	D_M	$D_{M\text{-}550°C}$	$D_{M\text{-}850°C}$
SiO_2	71.44	49.82	59.57	56.82
Fe_2O_3	6.22	18.20	20.30	20.72
Na_2O	2.61	7.64	8.44	8.31
Al_2O_3	1.64	8.46	9.21	9.59
K_2O	0.37	0.85	0.96	1.04
TiO_2	0.30	0.35	0.39	0.40
% LOI	17.42	14.68	1.13	3.12

The increased amount (71.44%) in the D_A sample showed the effect of acid washing. In addition, changes in the ratios of other compounds (Fe_2O_3, Na_2O, Al_2O_3, K_2O, and TiO_2) are observed. Since the diatomite samples consist of very different-sized particles, after acid treatment, they were transformed from the destroyed/broken oxide particles into crystallite/oxide complex compounds [23].

It was observed that ferrous chloride modified diatomite (D_M, $D_{M\text{-}550°C}$, and $D_{M\text{-}850°C}$) samples decreased SiO_2 contents (49.82%, 59.57%, and 56.82%, respectively). This could be explained

because the SiO_2 compound in the material composition produces sodium silicate (Na_2SiO_3) with NaOH since a 6 M NaOH solution is used during the modification process [24], [25]. Furthermore, the increase in Fe_2O_3 ratio (18.20%, 20.30%, and 20.72%, respectively) of D_M, $D_{M\text{-}550\ °C}$ and $D_{M\text{-}850\ °C}$ samples supports the modification process. In addition, especially after heat treatment, the loss of ignition rate is reduced. The volatile substances lost are usually hydrates, unstable hydroxy compounds, and carbon dioxide from carbonates. The new materials obtained with this decrease became more stable [26].

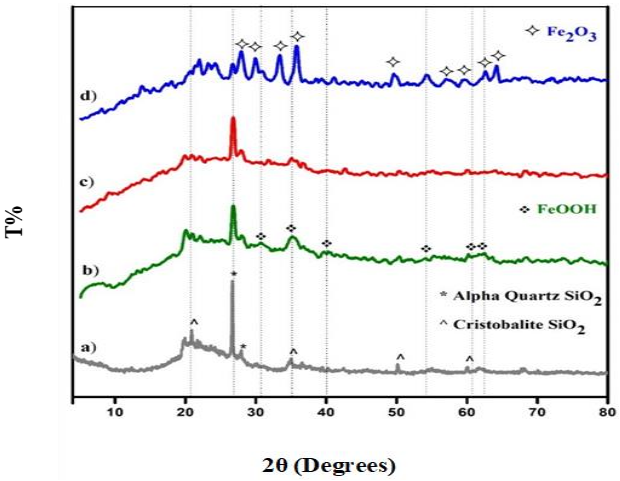

Figure 1. XRD patterns of a) D_A, b) D_M, c) $D_{M\text{-}550°C}$ and d) $D_{M\text{-}850°C}$.

The wide range of 2θ = 5–8°, 2θ = 18–28°, and at 2θ = 36° in the XRD pattern of the D_A sample indicated amorphous structure in Figure 1. A characteristic quartz peak of D_M, $D_{M\text{-}550°C}$, and $D_{M\text{-}850°C}$ were observed at 2θ = 26.72°, 26.84°, and 26.72°, respectively. Table S3. shows that the quartz structure maintains its dominance. However, in the data of D_M, $D_{M\text{-}550°C}$ and especially $D_{M\text{-}850°C}$, Fe_xO_y density increased, and again, the intensity of the characteristic quartz peak decreased in $D_{M\text{-}850°C}$. The obtained data are compatible with the studies presented in Table S3, and it was observed that the magnetic structures in the structure increased with modification, especially in the $D_{M\text{-}850°C}$ sample.

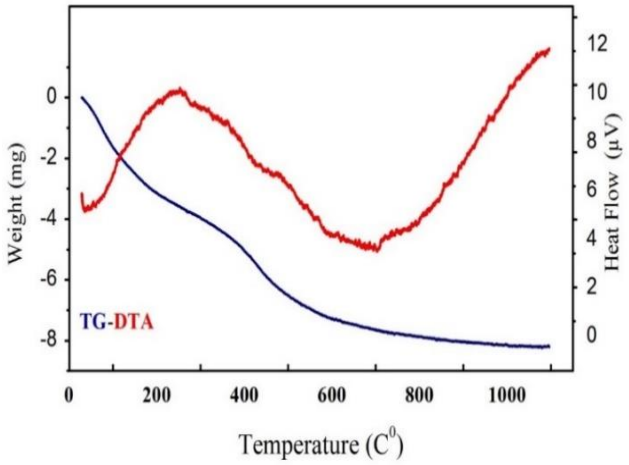

Figure 2. TG-DTA plots of D_A sample.

Thermogravimetric analysis (TG-DTA) was performed to determine the thermal degradation behavior and investigate the absolute stability. Only the TG-DTA thermogram of the DA sample was obtained between the samples prepared in the 25-1100 °C temperature range (Fig. 2). A three-step characteristic mass loss of diatomite is observed as the TG plot is examined. The dramatic mass loss (2.7%) between 25-100 °C was associated with mechanically trapped or physically adsorbed water. This peak depends, for example, on its morphological properties, such as surface area and particle size, rather than its chemical structure. Partially slow mass loss of between 120 and 360 °C (2.5%) was related to the nature of the opal phase, the hydrous silica with an irregular and amorphous structure, the main component of diatomite. The mass loss of 360- 920 °C (3.3%) was expressed by the decomposition of alkali metal and alkaline earth metal carbonates of diatomite. The sample did not decrease in weight upon further heating after 900 °C, indicating that the oxygenolysis process or decomposition reaction was complete. DTA curves were observed (Fig. 2), showing that two endothermic peaks appearing at 40 and 690 °C could be identified by dehydroxylation of silanol groups absorbed on diatomite and the outer surface of diatomite, respectively. Furthermore, at 260 °C, there was a solid exothermic peak due to the oxidation reactions of organic matter in the diatomite [27].

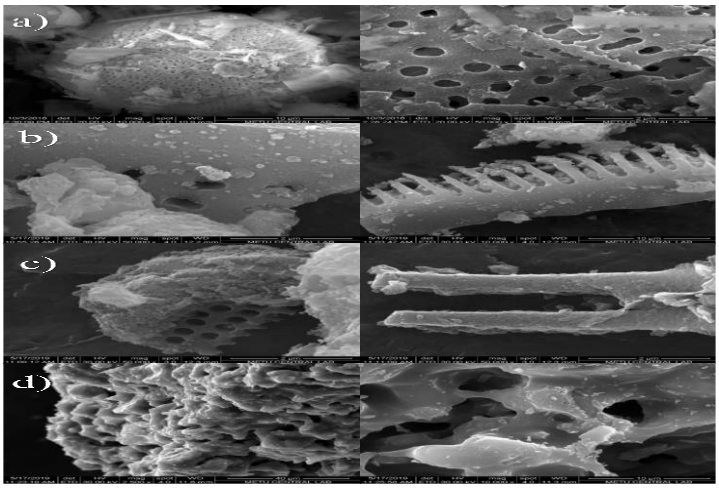

Figure 3. SEM micrographs of the D_A (a), D_M (b), $D_{M\text{-}550°C}$ (c) and $D_{M\text{-}850°C}$ (d).

In Figure 3, SEM morphologies of samples confirmed that diatomite particles consist of various morphologies such as a sphere, capsule, disc, and bilaterally symmetrical structure. The acid-washed (DA) diatomite sample was compared with the SEM image of the crude diatomite sample obtained in previous studies, and it was observed that the impurities accumulated in the pores were removed [16]. The SEM image of the ferrous chloride modified sample showed that the pores are enlarged and that some pores of the diatomite are filled and the rest are adsorbed on the surface of the diatomite. Following this treatment, in the 550 °C heat treated diatomite sample ($D_{M\text{-}550°C}$), the diatomite retained its partially skeletal structure; some pores were still open. Furthermore, it was seen that metallic salts are also agglomerated on the surface by the effect of the modification. It could be seen that the skeletal structure of the 850 °C heat treated diatomite ($D_{M\text{-}850°C}$) had completely changed and the spaces in the system had increased, as seen from the visual [28].

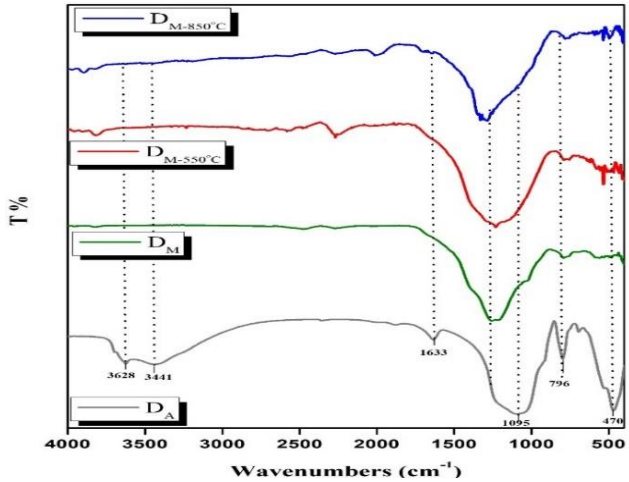

Figure 4. FTIR analysis of the D_A, D_M,$D_{M\text{-}550°C}$, and $D_{M\text{-}850°C}$.

The FTIR of the D_A sample is presented in Figure 4. The characteristic vibrational peaks of smectite were at 3628 cm^{-1} (O-H stretch), and the broadband centered at 3441 cm^{-1} and 1633 cm^{-1} was attributed to the -OH vibrational mode of physically adsorbed H_2O [29]. The peaks at 470 and 1095 cm^{-1} were from the asymmetric stress modes of Si–O–Si bonds; the weak absorption peaks at 695 cm^{-1}, and 796 cm^{-1} were probably due to Si–O deformation and Al–O stretching; and the peak at 800 cm^{-1} could be due to the stretching vibration of Al-O-Si [30], [31]. According to the FTIR results of the $D_{M\text{-}550°C}$ sample, the wide ~3400 cm^{-1} band disappeared when the sample temperature was increased to about 550 °C. The narrow band at ~3700 cm^{-1} was assigned to the strain mode of the free surface OH groups bound as Si–O–H [32].

The 3726 cm^{-1} shoulder band became denser after thermal treatment at 550 °C (Figure 4). At 850 °C (Figure 4), the band shifted to a lower wave number at 3780 cm^{-1} with increased symmetry and a significant decrease in intensity [33]. After thermal treatment, the density of the bands increased with water desorption and exposure to more silanol [34]. The results of the BET surface area analysis were summarized in Table S4; the BET surface area of the D_A sample increased by 12.5% compared to the original diatomite sample previously used. This increase could be due to cleaning the blocked pores by opening siloxane bridges with acid treatment [35]. The surface area of the D_M sample increased by 20.8%. The surface area increased with the removal of impurities and the opening of micropore areas due to the effect of the modification. The micropore areas (83.39 $m^2\ g^{-1}$) presented in Table S4 also support this. In the $D_{M\text{-}550°C}$ and $D_{M\text{-}850°C}$ samples, microporous walls could be destroyed by the effect of heat, and micro-pore width increased (37,12 Å and 58,84 Å)

and surface area decreased by 29% and 96%, respectively. The pore diameters obtained after the modification are presented in Table S4, and it was observed that the mesoporous (pore diameters in the range of 2-50 nm) structure dominates. The morphology analysis expected that the sample's surface area and pore volume would increase due to the porous structure [36]. However, during the thermal treatment at 850 °C, the blocked pores on the surface of the diatomite pores could not be determined by the BET N_2 adsorption method. Therefore, very low surface pore volume values were recorded with low surface area [37]. The data obtained from Matersizer analysis of samples with a wide variety of shapes are presented in Table S5, and the graphs are shown in Figure S1. In Figure S1, the size distribution of the D_A particles widened from 0.2 to 90 µm, and D (0.5) 32.01 µm was obtained. After the modification, the $D_{M\text{-}850°C}$ expanded as the size range (10 to 900 µm in Figure S1) increased as D (0.5): 135.1 µm and the main peak shifted to the right. D (0.5), median, diameter distribution and surface area, and volume width were highest at $D_{M\text{-}850°C}$, while specific surface area was lowest. This reduction in the specific surface area and the increased pore-size diameter after heating could be demonstrated by sintering [38].

3.2. Adsorption experiments

3.2.1. Effect of pH

The effect of pH on the adsorption of Co(II) by D_A, D_M, $D_{M\text{-}550°C}$, and $D_{M\text{-}850°C}$ is shown in Figure 5.

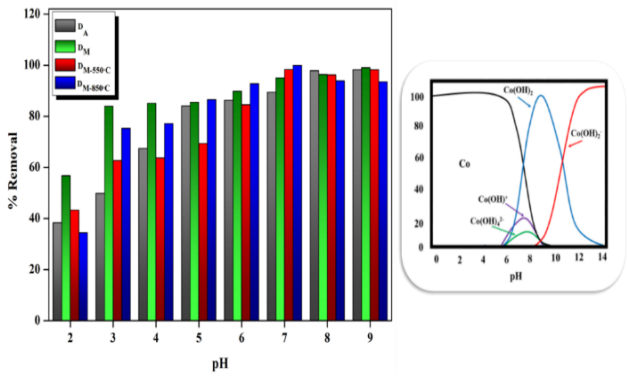

Figure 5. Effect of pH on the adsorption of Co(II) onto D_A, D_M, $D_{M\text{-}550°C}$ and $D_{M\text{-}850°C}$.

Another important factor affecting the adsorption capacity of the adsorbent is the pH of the solution. Therefore, the adsorption experiments for Co(II) were carried out under the conditions of C_0 = 30 mg L^{-1} and 298 K, ranging from pH 2 to 9. It increased between pH=4-8, as shown in Figure 5. The C=O and OH groups on the surface of the sample are more easily protonated under acidic conditions (< pH=7). It reduces the binding sites of the sample by causing them to bind with H^+ in the solution and prevents the adsorption of Co^{+2}. It is conceivable that as the pH of the solution increases from 4 to 8, more negative charges could be used for adsorption. At pH values > 8, Co^{+2} ions begin to precipitate as ions [39]. Therefore, a higher Co(II) adsorption capacity was obtained under pH=7 conditions.

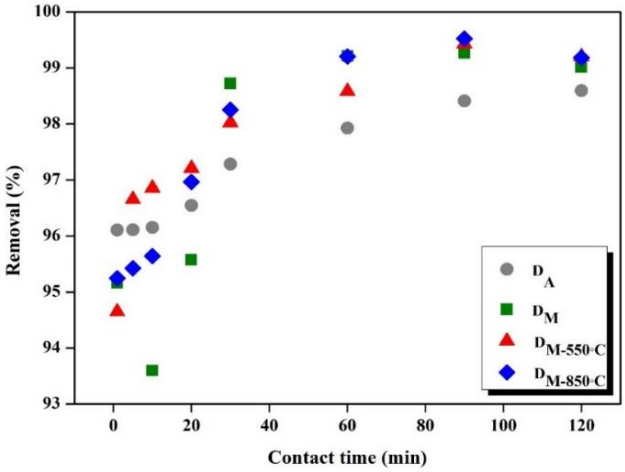

Figure 6. Effect of contact time on the adsorption of Co(II) onto D_A, D_M, $D_{M\text{-}550°C}$, and $D_{M\text{-}850°C}$.

The effect of contact time on the adsorption of Co(II) from aqueous solutions D_A, D_M, $D_{M\text{-}550°C}$ and $D_{M\text{-}850°C}$ samples was investigated. Figure 6 shows that the ion adsorption rate is constant due to a greater interaction with the vacant adsorption sites on the upper surface of the adsorbent, and then saturation occurs [40]. The removal of Co(II) ions from $D_{M\text{-}550°C}$ reached 94% at 10 minutes and its maximum (99.6%) after 90 minutes. Then the adsorption slowed down and reached equilibrium due to the reduced surface area that could be occupied by the adsorbate molecules.

3.3. Adsorption isotherm studies

Isotherm models (Langmuir, Freundlich, and Dubinin-Radushkevich) were used to describe the equilibrium between adsorbate and adsorbent systems (Figure 7), and correlation coefficients were calculated to assess the best fit (Table 2).

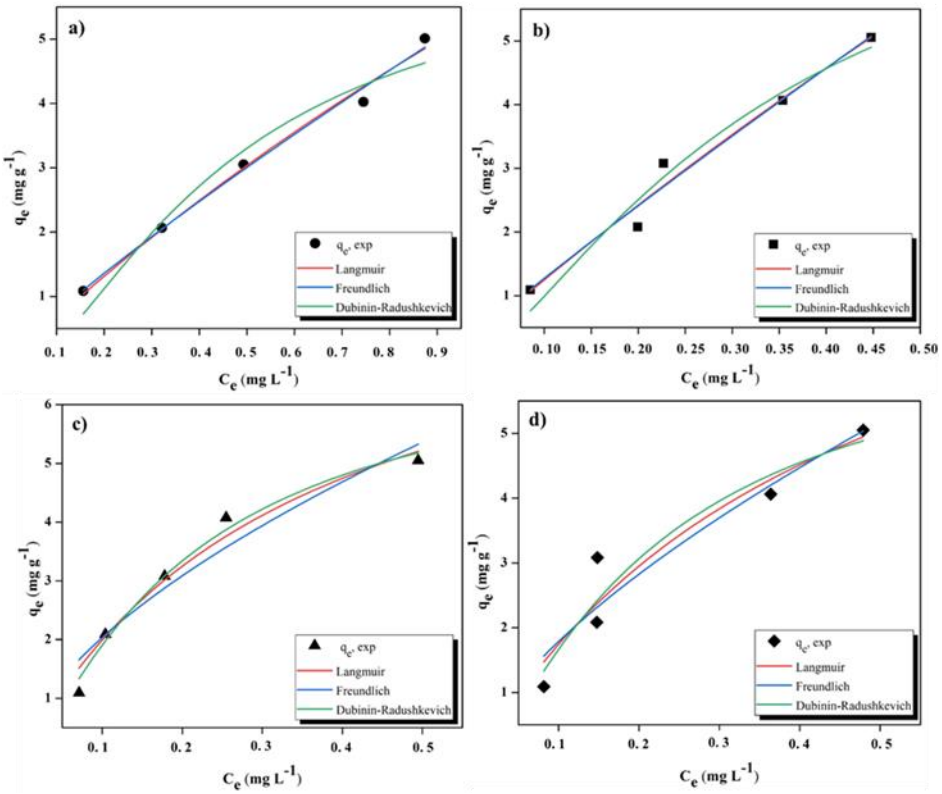

Figure 7. Adsorption nonlinear isotherm model for the D_A (a), D_M (b), $D_{M\text{-}550°C}$ (c) and $D_{M\text{-}850°C}$ (d).

Table 2. Isotherm parameters obtained by nonlinear fitting for the D_A (a), D_M (b), $D_{M\text{-}550°C}$ (c) and $D_{M\text{-}850°C}$ (d)

Isotherm/Model		D_A	SE	D_M	SE	$D_{M\text{-}550°C}$	SE	$D_{M\text{-}850°C}$	SE
Langmuir	**q_M (mg g^{-1})**	18.18	1.1581	28.65	0.5287	48.30	1.5358	66.22	0.3382
	K_L	0.4041	0.1622	0.4586	0.4492	0.3545	0.9333	0.2211	1.335
	R_L	0.1984		0.1790		0.2200		0.3114	
	R^2	0.9992		0.9813		0.9396		0.9091	
	X^2	0.0285		0.0791		0.1030		0.2632	
Freundlich	**K_F**	5.4853	0.1677	10.7920	1.2798	10.1953	1.1735	9.5214	1.4017
	1/n	0.8690	0.0766	0.9371	0.1345	0.7624	0.2941	0.7803	0.3156
	R^2	0.9969		0.9749		0.9146		0.8742	
	X^2	0.0247		0.0805		0.2295		0.2931	
Dubinin-Radushkevcih	**q_M (mg g^{-1})**	11.7190	0.6261	15.5897	1.0058	16.2665	0.3546	18.5100	0.8197
	$K_{D\text{-}R}$	0.0005	0.0953	0.0005	0.0582	0.0004	0.0181	0.0004	0.0476
	$E_{D\text{-}R}$	0.3162		0.3162		0.3536		0.3536	
	R^2	0.9941		0.9726		0.9376		0.8903	
	X^2	0.1313		0.1246		0.0435		0.2400	

The data for four nonlinear isotherm models are shown in Table 2. The values showed the fit of the Langmuir model to the experimental data, as it had higher R^2 values. In this study, the maximum adsorption capacities of D_A, D_M, $D_{M\text{-}550°C}$, and $D_{M\text{-}850°C}$ were 18.18 mg L^{-1}, 28.65 mg L^{-1}, 48.30 mg L^{-1}, and 66.22 mg L^{-1}, respectively. The constant K_L, separation factor R_L values related to the binding energy of the adsorption system, the best fit of the models to the experimental data, chi-square (χ^2), and error analysis (SE) are presented in Table 2. The Freundlich model shows a surface characterized by

multilayer inhomogeneous adsorption on the adsorbent surface. K_F (mg L-1) defines the amount of metal ions adsorbed on the adsorbent at equilibrium, while n measures the adsorption density or surface heterogeneity. The Freundlich model showed poor agreement with the experimental data for Co(II) metal ion at D_A, D_M, $D_{M\text{-}550°C}$, and $D_{M\text{-}850°C}$ (Fig. 7 A−D). The 1/n <1 values of the Freundlich model indicated that the adsorption levels were excellent. In this study, the n values are 0.8690 for D_A, 0.9371 for D_M, 0.7624 for $D_{M\text{-}550°C}$, and 0.7803 for $D_{M\text{-}850°C}$, which means proper adsorption. The Freundlich isotherm provided a less reasonable fit to the experimental data compared to the Langmuir models. On the other hand, the E values generated using the Dubinin–Radushkevich (D–R) model (E<8 kJ mol^{-1}, 298 K) were the values of samples that confirmed the physical adsorption behaviour (Table 2).

3.4. Adsorption kinetics studies

Kinetic models were used to test the experimental data to investigate the mechanism of adsorption of Co(II) to modified D_A, D_M, $D_{M\text{-}550°C}$, and $D_{M\text{-}850°C}$ and potential rate control steps such as mass transfer and chemical reactions. The adsorption kinetic model is usually defined by one of the following models: pseudo-first-order, pseudo-second-order, intraparticle diffusion model, and Boyd model.

Table 3. Kinetic parameters obtained using pseudo-first-order and pseudo-second-order kinetic models

Kinetic Models		D_A	D_M	$D_{M\text{-}550°C}$	$D_{M\text{-}850°C}$
	$q_{e\,(exp)}$ (mg g^{-1})	**3.0495**	**3.0761**	**3.0810**	**3.084**
Pseudo-first order	$q_{e.\,(cal)}$ (mg g^{-1})	0.1230	0.2586	0.1086	0.1353
	k_1 (min^{-1})	0.0519	0.0807	0.0234	0.0907
	R^2	0.8846	0.9199	0.9205	0.8753
Pseudo-second order	$q_{e.\,(cal)}$ (mg g^{-1})	3.0581	3.0807	3.0303	3.0845
	k_2 (g mg^{-1} min^{-1})	0.0093	0.0121	0.0095	0.0097
	R^2	1	1	1	1

Adsorption data were fitted using pseudo-first-order and pseudo-second-order kinetic models in Table 3. This fitting demonstrates that the pseudo-second-order kinetic model successfully describes the kinetics of Co(II) adsorption onto D_A, D_M, $D_{M\text{-}550°C}$, and $D_{M\text{-}850°C}$. Moreover, the q_e value was close to the experimental data calculated using the pseudo-first-order kinetic model, confirming that the studied adsorption systems belong to the pseudo-second-order kinetic model.

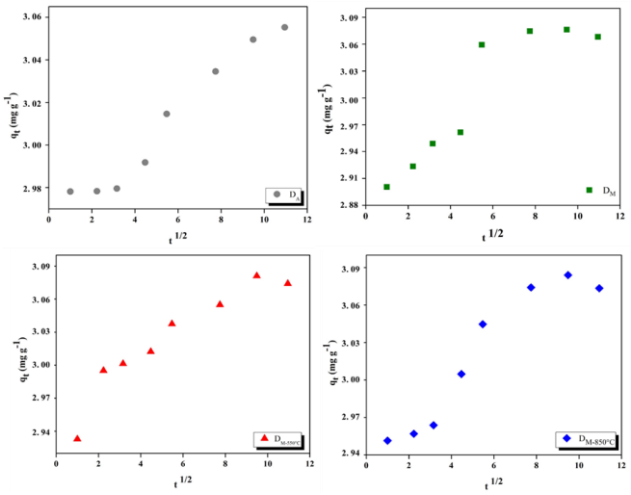

Figure 8. Intraparticle diffusion model for Co(II) adsorption onto theD_A, D_M, $D_{M\text{-}550°C}$ and $D_{M\text{-}850°C}$ samples.

Table 4. Intraparticle diffusion model data of Co(II) adsorption onto the D_A, D_M, $D_{M\text{-}550°C}$ and $D_{M\text{-}850°C}$ samples

İntraparticle Diffusion Model	**D_A**	**D_M**	**$D_{M\text{-}550°C}$**	**$D_{M\text{-}850°C}$**
k_i(mg L-1 $min^{-1(1/2)}$)	0.0123	0.03	0.0122	0.024
C (mg L-1)	2.9409	2.8545	2.963	2.8964
R^2	0.9351	0.8001	0.947	0.939

Figure 8 shows that the plot of q_t versus $t^{0.5}$ is an intraparticle diffusion model, indicating that three steps occurred. The boundary layer diffusion controlled the adsorption to some extent; as the drawing did not pass through the origin, it could be assumed that intraparticle diffusion was not the sole mechanism that controlled the adsorption. It could be concluded that three processes control the rate of adsorption of molecules, but only one was rate-limiting at any given time interval. The first process could be attributed to the diffusion of the bulk adsorbent to the outer surface, while the second process could be attributed to the diffusion into the mesopores. The third part was attributed to the equilibrium stage, where diffusion within the particles began to slow down due to the low concentration of chromium in the solution. The slope of the second linear section was defined as a velocity parameter (k_{in}) [41]. This range was characteristic of the adsorption rate, with intraparticle diffusion reported as the rate-limiting factor and the R^2 value ranging between 0.8001 and 0.9470 (Table 4).

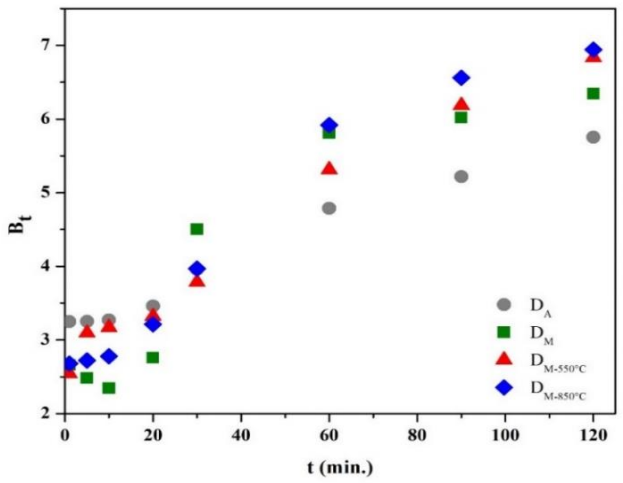

Figure 9. Boyd models of for Co(II) adsorption onto the D_A, D_M, $D_{M\text{-}550°C}$ and $D_{M\text{-}850°C}$ samples.

The plot of Bt versus t is called a Boyd plot in Figure 9, where a straight line through the origin means that the adsorption process is driven by diffusion within the particles. Otherwise, the adsorption process is controlled by either diffusion in the film or diffusion within the particles [42], [43]. From Figure 9, the plot did not pass through the origin, suggesting that film diffusion dominated the adsorption process.

3.7. Comparison with other adsorbents

Fu-qiang et al. (2013) investigated whether fly ash modified with ferrous chloride is an effective adsorbent in the removal of Mo(VI) from aqueous solutions. The adsorption equilibrium data agreed well with the Langmuir model, and the Langmuir adsorption capacity (Q_0) is 17.83 mg L^{-1}. They reported that the method is inexpensive, effective, and simple compared to existing treatment technologies [44]. Salmani et al. (2016), prepared activated carbon from pomegranate peel (PPC), modified it with $FeCl_3$ (Fe^{3+}PPC) and $FeCl_2$ (Fe^{2+}PPC) solutions, and studied the removal of Pb^{+2} from the aqueous solution. The maximum adsorption capacity estimated by the Langmuir model was 34.5 and 17.8 mg L^{-1} for Fe^{2+}PPC and Fe^{3+}PPC for Pb (II) ions, respectively. This was interpreted by the presence of chelating functional groups such as carboxyl, phenol, and OH on the Fe^{2+}PPC surface, which has a high affinity for removing Pb(II) ions [45]. Chunhui et al. (2018), obtained biochar (BC) using yak dung and modified it with $FeCl_2$ (Fe-BC3). Adsorption results showed that the maximum adsorption capacities of F^- and As (V) on Fe-BC3 were 3.928 mg L^{-1} and 2.926 mg L^{-1}, respectively [46]. Qi et al. (2020) studied how $FeCl_2$ was dissolved in anhydrous ethanol and further impregnated cotton textile waste (CTW) to prepare activated carbons (ACs) by pyrolysis. Afterwards, the physicochemical properties for ACs and adsorption capacities of Cr(VI) were evaluated. The maximum adsorption amount of AC-AE was 137.289 mg L^{-1} for Cr(VI). Also, in this study, it was emphasized that $FeCl_2$ exhibited better impregnation on raw materials compared to $FeCl_3$ [47].

3.8. Predicting mechanism of adsorption

Adsorption processes result in different adsorption interactions due to the various designs of adsorbents and consequent changing surface properties. It is explained by physical mechanisms such as van der Waals forces, hydrogen bonding, stacking, electrostatic interaction, and hydrophobic interaction. The chemical adsorption mechanism with more pronounced forces can also be effective due to the development of chemical bonds between the adsorbent and the adsorbate through electron sharing [48]. The more effective adsorption capacity of the modified samples may be the result of some important changes. In physisorption, the pore-filling effect may dominate due to the wide pore size distribution of heavy metals [49]. The adsorption of heavy metals on the surface of the adsorption material can cause a surface reaction. The pH of the aqueous solution is an important factor affecting the heavy metal species, the protonation of functional groups, the electric double layer on the surface, and the adsorption process. Its important effect on the heavy metal adsorption process is the protonation and deprotonation of hydroxyl groups in materials. According to the experimental results of pH change, electrostatic interactions could occur between positively charged adsorbates (Co(II)) and negatively charged functional groups containing residual oxygen [50]. Also, different fractions of Co(II) species could be an effective factor in pH environments. Surface complexation, including coordination and chelation, was an important mechanism for the removal of ionic species, mainly metal ions, from samples (in Fugure 10).

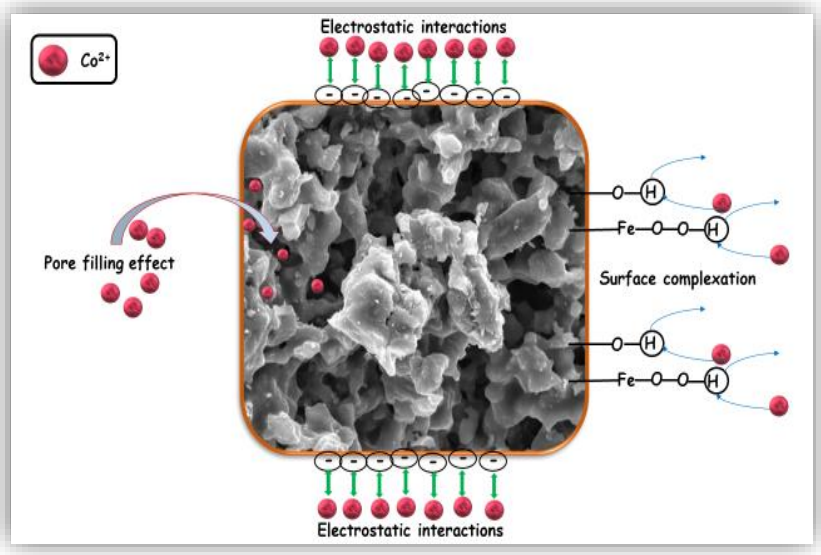

Figure 10. Plausible adsorption mechanism of Co (II) ions onto the D_A, D_M, $D_{M\text{-}550°C}$ and $D_{M\text{-}850°C}$ samples.

In the adsorption processes, the complex formation is strongly influenced by the pH of the solution, as it could involve the uptake/release of hydrogen ions [51]. The adsorption study showed that monolayer adsorption took place on the homogeneous surfaces of the samples. It could largely contribute to the adsorption behavior due to the domains provided by the oxygen-containing functional groups [52].

4. Conclusion

The aim of this study was to functionalize the surface of the adsorbent, which is a very effective method for removing waste from aqueous solutions. In this context, inspired by the previous work [18], it was modified with transition metal oxides, taking into account the high efficiency of the active groups on the surface, with ferrous chloride, and thermal treatment at two different temperatures (550 °C and 850 °C). In the elemental analysis, it was observed that the content of ferrous chloride ($FeCl_2$) compounds increased and became more stable as a result of the reduction of ignition rate loss with thermal treatment. It was noticed that the Fe_xO_y density increased with the modification according to the XRD pattern. It appeared that there were significant changes in pore structure and surface shape with modification, according to the SEM image. The change in samples with modification was supported by FTIR peaks. The results of the BET analysis and the Mastersizer analysis showed clear changes in the pore structure and the pore size distribution due to the effect of the modification. The pH of a solution is an important parameter affecting adsorption of metal ions on adsorbents. The adsorption capacities were measured at different pH values and pH=7 was found to be the most suitable for Co(II). The effect of time on the adsorption capacity was studied, and it was observed to reach equilibrium in approximately 90 minutes. From the correlation coefficients of the adsorption isotherms, the type of adsorption was more consistent with the Langmuir isotherm (R^2> 0.9). Also, it was found that $D_{M\text{-}850°C}$ adsorbed approximately 3.6 times better than D_A according to the adsorption capacities obtained from the Langmuir isotherm. It was found to be more compatible with the pseudo-second-order kinetics model using kinetic calculations. The adsorption processes of Co(II) on D_A, D_M, $D_{M\text{-}550°C}$, and $D_{M\text{-}850°C}$ samples were controlled by its monolayer and homogeneous surface, and physical adsorption, ion exchange, and electrostatic surface complexation were predicted to play a dominant role. It was concluded that ferrous chloride and thermally modified diatomite samples could be used as an effective, low-cost, and environmentally friendly adsorbent for the removal of Co(II) from an aqueous solution.

Contributions of the authors

Eda GÖKIRMAK SÖĞÜT: Conceptualization, methodology, investigation, writing-review&editing.

Metin ÇELEBİ: Conceptualization, methodology, investigation, visualization, writing-review&editing.

Data Availability Statement

The data that support the findings of this study are available in the supplementary material of this article.

Conflict of Interest Statement

There is no conflict of interest between the authors.

Statement of Research and Publication Ethics

The study is complied with research and publication ethics.

References

[1] M. Ferri, S. Campisi, and A. Gervasini, "Nickel and cobalt adsorption on hydroxyapatite: a study for the de-metalation of electronic industrial wastewaters," *Adsorption*, vol. 25, no. 3, pp. 649–660, Mar. 2019.

[2] L. P. Lingamdinne, J. R. Koduru, H. Roh, Y. L. Choi, Y. Y. Chang, and J. K. Yang, "Adsorption removal of Co(II) from waste-water using graphene oxide," *Hydrometallurgy*, vol. 165, pp. 90–96, Oct. 2016.

[3] Y. V. Hete, S. B. Gholase, and R. U. Khope, "Adsorption Study of Cobalt on Treated Granular Activated Carbon" *E-Journal Chem.*, vol. 9, no. 1, pp. 335–339, 2012.

[4] Y. Aşçi and Ş. Kaya, "Removal of cobalt ions from water by ion-exchange method" *New pub Balaban*, vol. 52, no. 1–3, pp. 267–273, 2014.

[5] F. L. Becker, D. Rodríguez, and M. Schwab, "Magnetic Removal of Cobalt from Waste Water by Ferrite Co-precipitation," *Procedia Mater. Sci.*, vol. 1, pp. 644–650, Jan. 2012.

[6] B. S. Thaçi and S. T. Gashi, "Reverse Osmosis Removal of Heavy Metalsfrom Wastewater Effluents Using BiowasteMaterials Pretreatment," *Polish J. Environ. Stud.*, vol. 28, no. 1, pp. 337–341, Nov. 2018.

[7] N. Tzanetakis, W. M. Taama, K. Scott, R. J. J. Jachuck, R. S. Slade, and J. Varcoe, "Comparative performance of ion exchange membranes for electrodialysis of nickel and cobalt," *Sep. Purif. Technol*, vol. 30, no. 2, pp. 113–127, Feb. 2003.

[8] Ö. Yavuz, Y. Altunkaynak, and F. Güzel, "Removal of copper, nickel, cobalt and manganese from aqueous solution by kaolinite," *Water Res.*, vol. 37, no. 4, pp. 948–952, Feb. 2003.

[9] N. Abdullah, N. Yusof, W. J. Lau, J. Jaafar, and A. F. Ismail, "Recent trends of heavy metal removal from water/wastewater by membrane technologies," *J. Ind. Eng. Chem.*, vol. 76, pp. 17–38, Aug. 2019.

[10] S. A. Mirbagheri and S. N. Hosseini, "Pilot plant investigation on petrochemical wastewater treatmentfor the removal of copper and chromium with the objective of reuse," *Desalination*, vol. 171, no. 1, pp. 85–93, Jan. 2005.

[11] Y. Huang, X. Zeng, L. Guo, J. Lan, L. Zhang, and D. Cao, "Heavy metal ion removal of wastewater by zeolite-imidazolate frameworks," *Sep. Purif. Technol.*, vol. 194, pp. 462–469, Apr. 2018.

[12] M. Çelebi and E. Gökirmak Söğüt, "High-efficiency removal of cationic dye and heavy metal ions from aqueous solution using amino-functionalized graphene oxide, adsorption isotherms, kinetics studies, and mechanism," *Turkish J. Chem.*, vol. 46, no. 5, pp. 1577–1593, Jan. 2022.

[13] H. Peng and J. Guo, "Removal of chromium from wastewater by membrane filtration, chemical precipitation, ion exchange, adsorption electrocoagulation, electrochemical reduction, electrodialysis, electrodeionization, photocatalysis and nanotechnology: a review," *Environ. Chem. Lett.* 186, vol. 18, no. 6, pp. 2055–2068, Jul. 2020.

[14] E. S. Gokirmak and N. K. Caliskan, "Removal of lead, copper and cadmium ions from aqueous solution using raw and thermally modified diatomite," *Desalin. Water Treat.*, vol. 58, pp. 154–167, Jan. 2017.

[15] Y. Fu, X. Xu, Y. Huang, J. Hu, Q. Chen, and Y. Wu, "Preparation of new diatomite–chitosan composite materials and their adsorption properties and mechanism of Hg(II)," *R. Soc. Open Sci.*, vol. 4, no. 12, Dec. 2017.

[16] E. S. Gökırmak and N. K. Çalışkan, "Isotherm and Kinetic Studies of Pb(II) Adsorption on Raw And Modified Diatomite By Using Non-Linear Regression Method," *Fresenius Environ. Bull.*, vol. 26, no. 4, pp. 2720–2728, 2017.

[17] M. Šljivić, I. Smičiklas, S. Pejanović, and I. Plećaš, "Comparative study of Cu2+ adsorption on a zeolite, a clay and a diatomite from Serbia," *Appl. Clay Sci.*, vol. 43, no. 1, pp. 33–40, Jan. 2009.

[18] N. K. Çalışkan, A. R. Kul, S. Alkan, E. S. Gökırmak, and I. Alacabey, "Adsorption of Zinc(II) on diatomite and manganese-oxide-modified diatomite: A kinetic and equilibrium study," *J. Hazard. Mater.*, vol. 193, pp. 27–36, Oct. 2011.

[19] E. S. Gökırmak and N. K. Çalışkan, "Equilibrium and Kinetic Studies of a Cationic Dye Adsorption onto Raw Clay," J. Turk.Chem.Soc. Sect. Chem., vol. 7, no. 3, pp. 713-720, 2020.

[20] S. By and W. Xiong, "Development and application of ferrihydrite-modified diatomite and gypsum for phosphorus control in lakes and reservoirs," 2009.
[21] W. Xiong and J. Peng, "Development and characterization of ferrihydrite-modified diatomite as a phosphorus adsorbent," *Water Res.*, vol. 42, no. 19, pp. 4869–4877, Dec. 2008.
[22] W. Xiong, J. Peng, Y. Hu, W. Xiong, J. Peng, and Y. Hu, "Chemical analysis for optimal synthesis of ferrihydrite-modified diatomite using soft X-ray absorption near-edge structure spectroscopy," *PCM*, vol. 36, no. 10, pp. 557–566, Dec. 2009.
[23] R. Goren, T. Baykara, and M. Marsoglu, "A study on the purification of diatomite in hydrochloric acid," *Scand. J. Metall.*, vol. 31, no. 2, pp. 115–119, Apr. 2002.
[24] M. K. Faizi, A. B. Shahriman, M. S. A Majid, al -, K. Progo, and Y. Fahmiati, "Characteristics of Iron Sand Magnetic Material from Bugel Beach, Kulon Progo, Yogyakarta," *IOP Conf. Ser. Mater. Sci. Eng.*, vol. 172, no. 1, p. 012020, Feb. 2017.
[25] J. M. Rimsza, R. E. Jones, and L. J. Criscenti, "Interaction of NaOH solutions with silica surfaces," *J. Colloid Interface Sci.*, vol. 516, pp. 128–137, Apr. 2018.
[26] O. Heiri, A. F. Lotter, and G. Lemcke, "Loss on ignition as a method for estimating organic and carbonate content in sediments: reproducibility and comparability of results," *J. Paleolimnol.* 2001 251, vol. 25, no. 1, pp. 101–110, 2001.
[27] R. Zheng, Z. Ren, H. Gao, A. Zhang, and Z. Bian, "Effects of calcination on silica phase transition in diatomite," *J. Alloys Compd.*, vol. 757, pp. 364–371, Aug. 2018.
[28] Q. Zhang, T. Zhang, T. He, and L. Chen, "Removal of crystal violet by clay/PNIPAm nanocomposite hydrogels with various clay contents," *Appl. Clay Sci.*, vol. 90, pp. 1–5, Mar. 2014.
[29] J. Madejová, W. P. Gates, and S. Petit, "IR Spectra of Clay Minerals," *Dev. Clay Sci.*, vol. 8, pp. 107–149, Jan. 2017.
[30] H. Aguiar, J. Serra, P. González, and B. León, "Structural study of sol–gel silicate glasses by IR and Raman spectroscopies," *J. Non. Cryst. Solids*, vol. 355, no. 8, pp. 475–480, Apr. 2009.
[31] B. B. Zviagina, V. A. Drits, and O. V. Dorzhieva, "Distinguishing Features and Identification Criteria for K-Dioctahedral 1M Micas (Illite-Aluminoceladonite and Illite-Glauconite-Celadonite Series) from Middle-Infrared Spectroscopy Data," *Miner.* 2020, Vol. 10, Page 153, vol. 10, no. 2, p. 153, Feb. 2020.
[32] B. A. Gaweł, A. Ulvensøen, K. Łukaszuk, A. M. F. Muggerud, and A. Erbe, "In situ high temperature spectroscopic study of liquid inclusions and hydroxyl groups in high purity natural quartz," *Miner. Eng.*, vol. 174, p. 107238, Dec. 2021.
[33] K. Khivantsev, N. R. Jaegers, L. Kovarik, M. A. Derewinski, J. H. Kwak, and J. Szanyi, "On the Nature of Extra-Framework Aluminum Species and Improved Catalytic Properties in Steamed Zeolites," *Mol.* 2022, Vol. 27, Page 2352, vol. 27, no. 7, p. 2352, Apr. 2022.
[34] L. T. Zhuravlev, "The surface chemistry of amorphous silica. Zhuravlev model," *Colloids Surfaces A Physicochem. Eng. Asp.*, vol. 173, no. 1–3, pp. 1–38, Nov. 2000.
[35] C. E. Fowler, C. Buchber, B. Lebeau, J. Patarin, C. Delacôte, and A. Walcarius, "An aqueous route to organically functionalized silica diatom skeletons," *Appl. Surf. Sci.*, vol. 253, no. 12, pp. 5485–5493, Apr. 2007.
[36] X. Ye *et al.*, "Modified natural diatomite and its enhanced immobilization of lead, copper and cadmium in simulated contaminated soils," *J. Hazard. Mater.*, vol. 289, pp. 210–218, May 2015.
[37] M. Aivalioti, I. Vamvasakis, and E. Gidarakos, "BTEX and MTBE adsorption onto raw and thermally modified diatomite," *J. Hazard. Mater.*, vol. 178, no. 1–3, pp. 136–143, Jun. 2010.
[38] S. M. Glasauer, P. Hug, P. G. Weidler, and A. U. Gehring, "Inhibition of Sintering by Si During the Conversion of Si-Rich Ferrihydrite to Hematite," *Clays Clay Miner.* 2000 481, vol. 48, no. 1, pp. 51–56, Feb. 2000.
[39] Ç. Üzüm, T. Shahwan, A. E. Eroğlu, I. Lieberwirth, T. B. Scott, and K. R. Hallam, "Application of zero-valent iron nanoparticles for the removal of aqueous Co^{2+} ions under various experimental conditions," *Chem. Eng. J.*, vol. 144, no. 2, pp. 213–220, Oct. 2008.
[40] V. Srivastava and M. Sillanpää, "Synthesis of malachite@clay nanocomposite for rapid scavenging of cationic and anionic dyes from synthetic wastewater," *J. Environ. Sci.*, vol. 51, pp. 97–110, Jan. 2017.
[41] Y. H. Magdy and H. Altaher, "Kinetic analysis of the adsorption of dyes from high strength wastewater on cement kiln dust," *J. Environ. Chem. Eng.*, vol. 6, no. 1, pp. 834–841, Feb. 2018.
[42] C. Yao and T. Chen, "A film-diffusion-based adsorption kinetic equation and its application," *Chem. Eng. Res. Des.*, vol. 119, pp. 87–92, Mar. 2017.

[43] K. K. H. Choy, D. C. K. Ko, C. W. Cheung, J. F. Porter, and G. McKay, "Film and intraparticle mass transfer during the adsorption of metal ions onto bone char," *J. Colloid Interface Sci*., vol. 271, no. 2, pp. 284–295, Mar. 2004.

[44] W. Fu-Qiang, L. Jian-Jun, and Z. Yi-Min, "Batch and column study: adsorption of Mo(VI) from aqueous solutions using $FeCl_2$-modified fly ash," *New pub Balaban*, vol. 51, no. 28–30, pp. 5727–5734, 2013.

[45] M. H. Salmani, M. Abedi, and S. A. Mozaffari, "Adsorption Efficiency of Iron Modified Carbons for Removal of Pb(II) Ions from Aqueous Solution," *J. Community Heal. Res*., vol. 5, no. 2, pp. 140–148, 2016.

[46] L. Chunhui, T. Jin, Z. Puli, Z. Bin, B. Duo, and L. Xuebin, "Simultaneous removal of fluoride and arsenic in geothermal water in Tibet using modified yak dung biochar as an adsorbent," *R. Soc. Open Sci*., vol. 5, no. 11, Nov. 2018.

[47] R. Qi *et al.*, "Effect of dispersant on the synthesis of cotton textile waste–based activated carbon by $FeCl_2$ activation: characterization and adsorption properties," *Environ. Sci. Pollut. Res*., vol. 27, no. 36, pp. 45175–45188, Dec. 2020.

[48] C. E. R. Barquilha and M. C. B. Braga, "Adsorption of organic and inorganic pollutants onto biochars: Challenges, operating conditions, and mechanisms," *Bioresour. Technol. Reports*, vol. 15, p. 100728, Sep. 2021.

[49] M. Choudhary, R. Kumar, and S. Neogi, "Activated biochar derived from Opuntia ficus-indica for the efficient adsorption of malachite green dye, Cu^{+2} and Ni^{+2} from water," *J. Hazard. Mater*., vol. 392, p. 122441, Jun. 2020.

[50] B. Zhao, X. Xu, R. Zhang, and M. Cui, "Remediation of Cu(II) and its adsorption mechanism in aqueous system by novel magnetic biochar derived from co-pyrolysis of sewage sludge and biomass," *Environ. Sci. Pollut. Res*., vol. 28, no. 13, pp. 16408–16419, Apr. 2021.

[51] X. Zhao, H. Feng, P. Jia, Q. An, and M. Ma, "Removal of Cr(VI) from aqueous solution by a novel ZnO-sludge biochar composite," *Environ. Sci. Pollut. Res*., vol. 1, pp. 1–15, Jun. 2022.

[52] E. Gökırmak Söğüt, "Effect of Chemical and Thermal Treatment Priority on Physicochemical Properties and Removal of Crystal Violet Dye from Aqueous Solution," *Chemistry Select*, vol. 7, no. 19, p. e202200262, May 2022.